Supplementary Information: Visible-Light-Driven Rotation of Molecular Motors in a Dual-Function Metal-Organic Framework Enabled by Energy Transfer.

Wojciech Danowski,[a] Fabio Castiglioni,[b] Andy S. Sardjan,[d] Simon Krause,[a] Lukas Pfeifer,[a] Diederik Roke,[a] Angiolina Comotti,[b] Wesley R. Browne,[a,c,*] Ben L. Feringa[a,*]

Correspondence: W.R.Browne@rug.nl, B.L.Feringa@rug.nl

a Centre for Systems Chemistry, Stratingh Institute for Chemistry, University of Groningen, Nijenborgh 4, 9747 AG, Groningen, The Netherlands.

b Department of Materials Science, University of Milano Bicocca, 20125 Milan, Via R. Cozzi 55, Milano, Italy

c Molecular Inorganic Chemistry Group, Stratingh Institute for Chemistry, University of Groningen, Nijenborgh 4, 9747AG Groningen, The Netherlands

Table of Contents

1. General Information

All reagents were obtained from commercial sources: Pd-meso-tetra(4-carboxyphenyl)porphyrin (**PdTCPP**, Frontier Scientific®), meso-α,β-Di(4-pyridyl) glycol (**DPG**, TCI), DMF (Acros Organics), absolute ethanol (Biosolve), HBF_4 (48 wt% in H_2O, Sigma-Aldrich) $Zn(NO_3)_2 \cdot 6H_2O$ (Sigma-Aldrich) and used as received without further purification. Molecular motor **1** was synthesized according to a literature procedure.[1] Elemental (C,H,N) Analysis was performed on an Elementar Vario MICRO cube: Elemental Analyzer, ICP-OES was performed on a PerkinElmer optical emission spectrometer Optima 7000 DV. NMR spectra were obtained using a Varian Mercury Plus (^{1}H: 400 MHz, ^{13}C: 100 MHz), Bruker Avance NEO (^{1}H: 600 MHz, ^{13}C: 150 MHz) or Varian Innova (^{1}H: 500 MHz) instruments. Chemical shifts are reported in δ units (ppm) relative to the residual solvent signal of DMSO-d_6 (^{1}H NMR, δ 2.50 ppm; ^{13}C NMR, δ 39.5 ppm) or THF-d_8 (^{1}H NMR, δ 1.72 ppm, 3.58 ppm). The splitting pattern is designated as follows: s (singlet), d (doublet), t (triplet), m (multiplet), br (broad), p (quintet), dd (doublet of doublets) ddd (doublet of doublets of doublets). UV/Vis absorption spectra were measured on a Hewlett-Packard 8453 diode array spectrometer in a 1 cm quartz cuvette. The Raman spectra were recorded on home-built system comprising a 1064 nm (Cobolt RumbaTM) 500 mW laser, equipped with Raman probe (250 $mW \cdot cm^{-1}$ transmitted power density) and connected to spectrograph (Andor™ Technology, SR-303I-B). Raman spectra at 785 nm were recorded using a PerkinElmer RamanStation400F with 80 mW at sample. The steady-state emission spectra of solid samples and in solution were recorded on Spectrofluorometer FS5 (Edinburgh Instruments) equipped with SC-20 sample holder. Phosphorescence quantum yields were determined using Spectrofluorometer FS5 (Edinburgh Instruments) equipped with SC-30 integrating sphere. The phosphorescence lifetimes in solution were determined using Spectrofluorometer FS5 (Edinburgh Instruments) equipped with SC-20 sample holder. The phosphorescence lifetimes of solid MOFs were recorded on home-built system comprising 532 nm excitation laser (SpitLight 400, InnoLas) and Omni-λ 300 (Zolix) monochromator/spectrograph and digital phosphor oscilloscope (DPO 4032, Tektronix). All the irradiation experiments were performed using Thorlab LEDs (M530F2 530 nm Thorlab LED). Solvents used for spectroscopic studies were of spectroscopic grade (UVASOL, Merck). PXRD data were obtained a Bruker D8 Advance diffractometer equipped with a Cu Kα source (λ = 0.15406 nm) in a Debye-Scherrer geometry. SC Xray data was collected using Bruker-AXS D8 Venture diffractometer with rotating anode and Cu radiation (λ = 1.54184 Å) at a temperature of 100(2).

2. Synthetic Procedures

Synthesis of the PdTCPP-DPG MOF. A 4 mL screw-cap glass vial was loaded with 4.45 mg (4.97 μmol, 1.0 equiv.) of **PdTCPP**, 2.15 mg (9.94 μmol, 2.0 equiv.) of **DPG**, 40 μL of stock solution (110 mg in 1 mL of EtOH) of $Zn(NO_3)_2 \cdot 6H_2O$ (4.43 mg, 14.8 μmol, 3.0 equiv.) and 32 μL of HBF_4 stock solution in EtOH (prepared by dilution of 100 μL of 48% aqueous HBF_4 acid in 1mL of EtOH) and diluted with 0.75 mL of DMF and 0.25 mL of EtOH. The mixture was sonicated in an ultrasonic bath for complete dissolution and placed in 80 ºC in an oven for 24 h upon which plate shaped deep purple crystals were formed. The crystals were collected and washed thoroughly with DMF yielding ca. 5 mg of dried crystals (after removal of DMF). For large scale synthesis (up to 89 mg of **PdTCPP**) the starting materials were mixed in appropriate ratios in a larger vial and split evenly into 1 mL batches. For ^{1}H NMR studies the sample was washed thoroughly with DCM and dried in vacuum to remove most of the solvent from the pores of the material, next 0.5 mL of DMSO-d_6 with 3 drops of D_2SO_4 were added and the sample was sonicated until full dissolution of the material. ^{1}H NMR (600 MHz, DMSO-d_6) δ (ppm) 8.82 – 8.77 (m, 4H), 8.67 (s, 8H), 8.26 (d, J = 7.8 Hz, 8H), 8.16 (d, J = 7.8 Hz, 8H), 7.96 – 7.92 (m, 4H), 4.91 (s, 2H). Elemental Analysis calcd. [**PdTCPP-DPG**-Zn_2•1.8 DMF•0.6 H_2O] %C 56.90, %H 3.64, %N 7.92, %Zn 9.47, %Pd 7.71 found %C 56.46, %H 3.13, %N 8.34, %Zn

9.95, %Pd 7.93. The needle shaped crystals (see Figure S7 for optical micrograph and SC-Xray structure) of the interpenetrated **PdTCPP-DPG** MOF were grown following an analogous procedure with 16 μL of the aforementioned HBF_4 stock solution.

Synthesis of motorized MOF via SALE. Crystals of parent **PdTCPP-DPG** MOF (approximately 5 mg) were placed in a 4 mL screw cap vial, and larger patches of crystals were gently pulverized with a Pasteur pipette, and 1 mL solution of molecular motor **1** (approximately 20 mg) in DMF was added. The vial was kept in the oven at 80 ºC for 24 h after which, the solution of molecular motor **1** was replaced by a fresh one and the exchange was continued for further 24 h at 80 ºC. Next, the crystals were washed thoroughly with DMF and kept under solvent for further studies. For ^{1}H NMR studies the sample was washed thoroughly with DCM and dried in vacuum to remove most of the solvent from the pores of the material, next 0.5 mL of DMSO-d_6 with 3 drops of D_2SO_4 were added and the sample was sonicated until full dissolution of the material. ^{1}H NMR (600 MHz, DMSO-d_6) 9.02 – 8.98 (m, 2H), 8.76 (s, 8H), 8.69 – 8.65 (m, 2H), 8.59 – 8.55 (m, 2H), 8.42 (s, 1H), 8.38 (d, J = 8.1 Hz, 1H), 8.33 (d, J = 8.1 Hz, 8H), 8.30 (d, J = 8.0 Hz, 1H), 8.28 – 8.23 (m, 8H), 8.19 (dd, J = 18.7, 8.3 Hz, 2H), 8.12 (dd, J = 8.0, 1.5 Hz, 1H), 7.97 (dd, J = 8.0, 1.7 Hz, 1H), 7.76 (d, J = 8.3 Hz, 1H), 7.62 – 7.56 (m, 2H), 7.40 (ddd, J = 8.2, 6.7, 1.3 Hz, 1H), 7.26 – 7.22 (m, 2H), 7.00 (d, J = 1.7 Hz, 1H), 4.51 (q, J = 6.6 Hz, 1H), 3.60 (dd, J = 15.6, 5.5 Hz, 1H), 2.92 – 2.84 (m, 1H), 1.43 (d, J = 6.7 Hz, 3H). Elemental Analysis calcd. [**1-PdTCPP**-Zn_2•0.8 DMF•1.5 DCM] %C 62.57, %H 3.47, %N 5.58, %Zn 7.66, %Pd 6.23 found %C 62.79, %H 3.69, %N 5.30, %Zn 7.20, %Pd 5.50. For SC-Xray crystals of the parent MOF were not pulverized and the exchange was also carried out for two days.

3. Experimental Procedures

UV/Vis studies. For the UV/Vis studies solutions were degassed by sparging with argon for ca. 1 min in a 1 cm quartz cuvette equipped with a septum-sealed screw cap. For the kinetic studies solutions were irradiated at 530 nm at a range of temperatures (6–14 °C, every 2 °C) until no further changes were observed in the UV/Vis spectrum. The irradiation was discontinued and the changes in absorbance at 440 nm were followed in time. For the alternating irradiation and thermal helix inversion cycles the solutions were irradiated at RT until no further changes were observed in the UV/Vis spectrum and kept at RT in the dark for the thermal process.

^{1}H NMR analysis. For the *in situ* ^{1}H NMR studies the solution of **PdTCPP** and **1** (3.0 mmol for both components) in THF-d_8 was purged in the NMR tube with argon for ca. 30 sec, submerged with an Evans NMR tube equipped with optical fibre and sealed with Parafilm.

Raman Studies. In solution Raman spectra were recorded in 1 cm quartz cuvette equipped with a tightly sealed screw cap in a sample holder equipped with a TC1 temperature controller (Quantum Northwest). The equimolar solution of **PdTCPP** and **1** (15.0 mM, DMF, ca. 1 mL) was degassed in the cuvette by purging with Argon and irradiated at 530 nm with stirring for approximately 30 min at –20 °C to reach PSS. Subsequently, the solution was warmed up to room temperature to facilitate the thermal helix inversion. In solid, DMF wet samples of **DPG** and motorized **PdTCPP** MOFs were placed between two quartz slides and sealed with Teflon tape to prevent drying. For variable power experiments power of the laser was tuned by changing the aperture of the slit and the transmitted power was measured using using a FieldMate laser power meter (RoHS compliant).

Emission Studies. For emission studies in solution DMF was degassed by five freeze-pump-thaw cycles and placed inside a glovebox. All the solutions were prepared innside a glove box in a 1 cm quartz cuvettes equipped with a septum-sealed screw cap by dilution of the same DMF stock solutions of **PdTCPP** and molecular motor **1** to a final concentration of **PdTCPP** of 44.6 μM. For emission studies in the solid, a suspension of **PdTCPP-DPG** or motorized **PdTCPP** MOFs crystals in DMF

were placed in a Φ = 5 mm NMR tube equipped with J. Young valve and degassed by 5 freeze-pump-thaw cycles.

Elemental Analysis. For elemental analysis MOFs samples were washed thoroughly with DMF then with DCM, dried and kept under a vacuum for 24 h prior to the analysis.

PXRD Studies. PXRD data of MOFs was collected for samples enclosed in spinning glass 1.0 mm capillaries (Hampton Research, HR6-122) with supernatant liquid. MOFs crystals were gently ground with a glass Pasteur pipette and transferred to the capillaries which were subsequently sealed with wax and placed on the goniometer head for mounting on the diffractometer.

4. ^{1}H NMR Spectra

a. ^{1}H NMR Data of the Digested MOFs

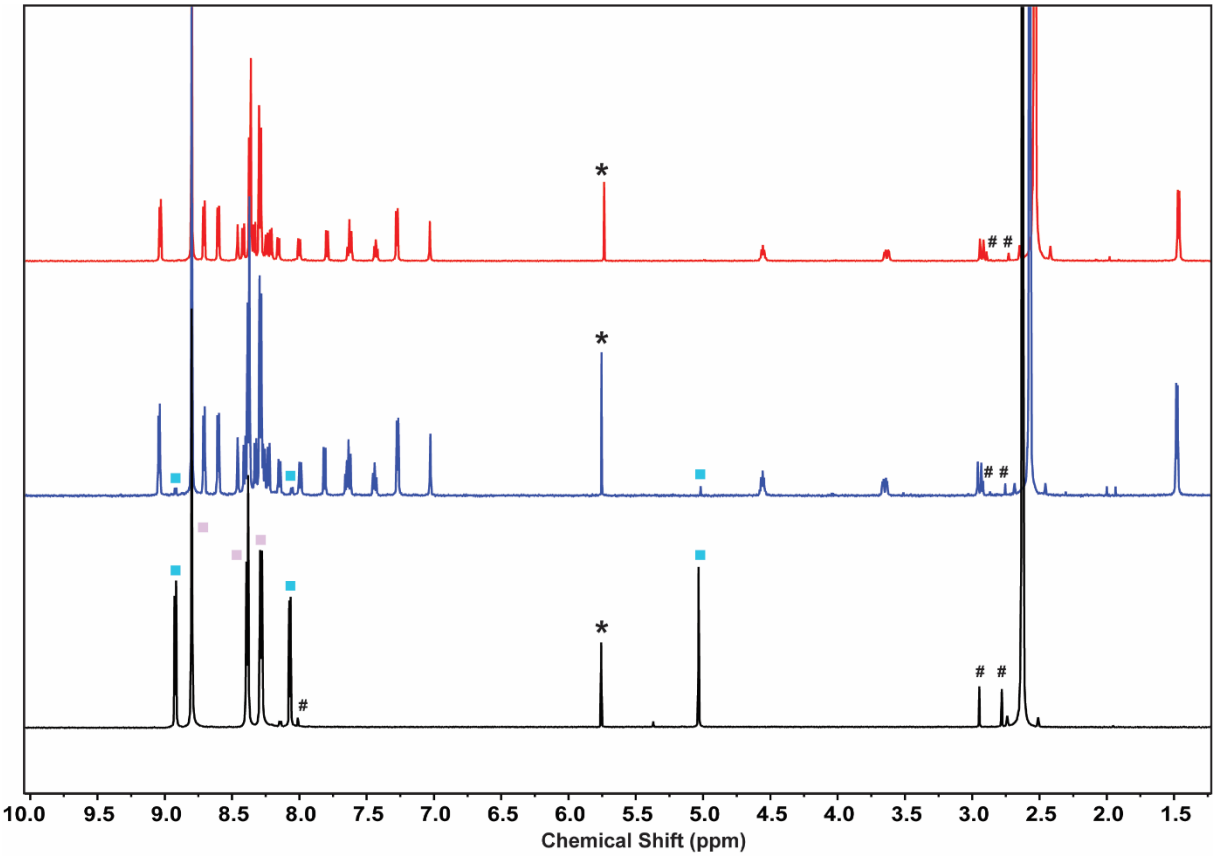

Figure S1 Comparison of the ^{1}H NMR (600 MHz, DMSO-d_6) spectra of the digested (D_2SO_4) crystals of parent **PdTCPP-DPG** MOF (black spectrum), motorized MOF after 24 h of exchange with **1** (blue spectrum) and motorized MOF after another 24 h of exchange (red spectrum). Resonances characteristic of **DPG** pillar are marked with blue squares, characteristic of the **PdTCPP** linker pink squares and residual solvents DMF and DCM are marked with number sign and asterisk respectively. Integration of the residual **DPG** aliphatic signal indicated 96% of exchange after 24 h. Note that the solvent residual signal shifts inconsistently due to the protonation of the DMSO and therefore spectra were referenced to PdTCPP resonances.

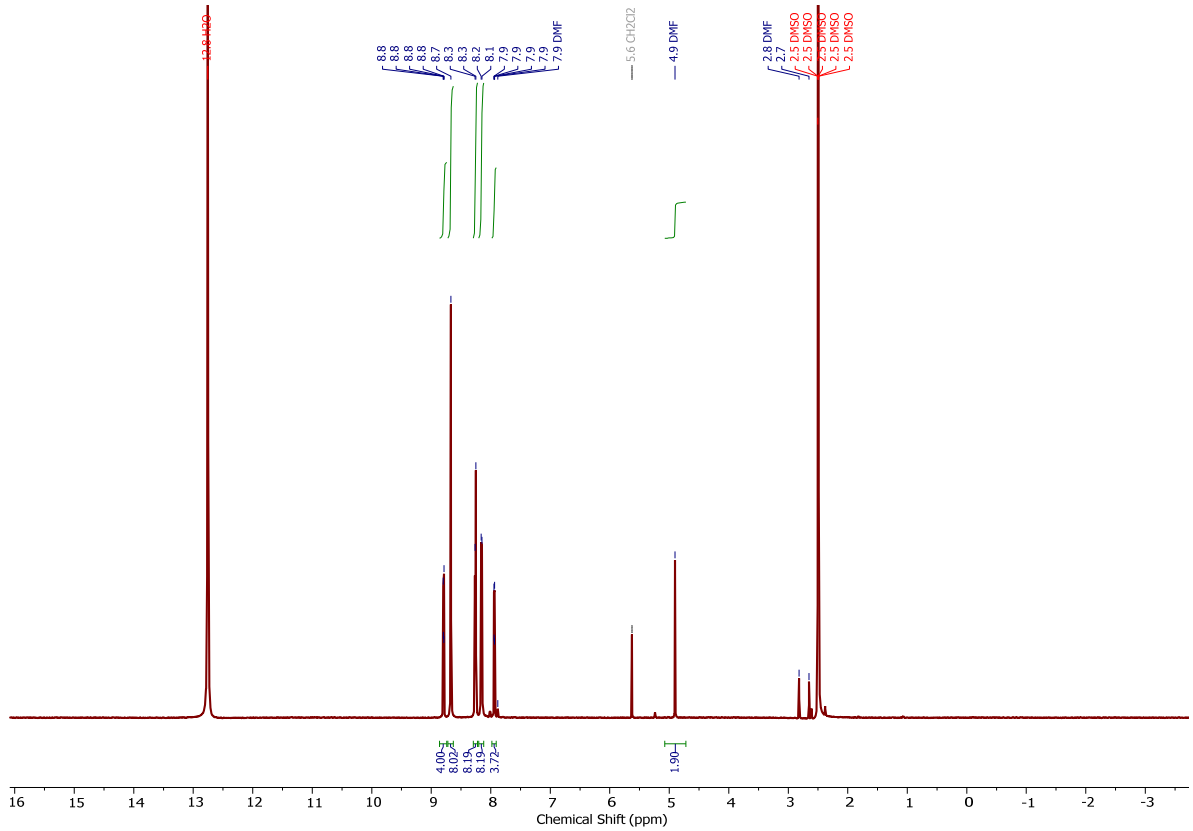

Figure S2 ^{1}H NMR (600 MHz, DMSO-d_6) spectrum of the digested (D_2SO_4) crystals of parent **PdTCPP-DPG** MOF.

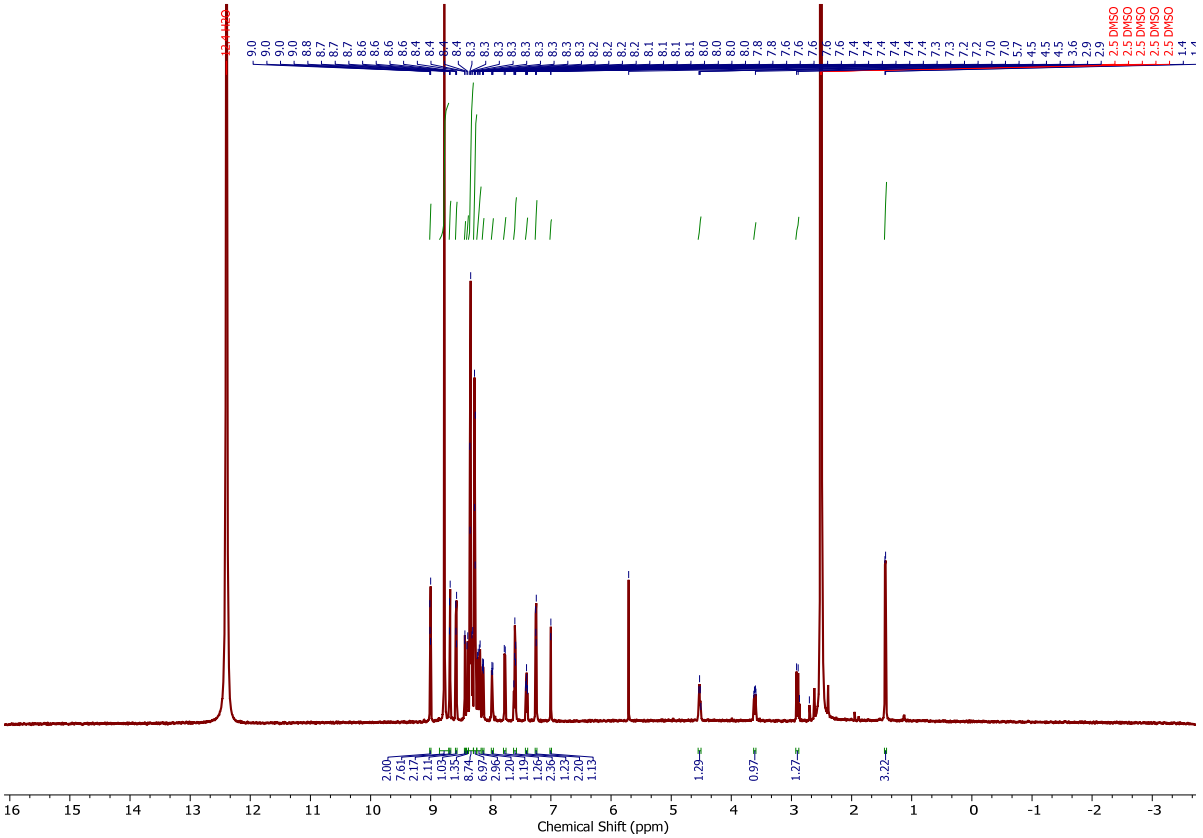

Figure S3 ^{1}H NMR (600 MHz, DMSO-d_6) spectrum of the digested (D_2SO_4) crystals of motorized **PdTCPP-1** MOF.

b. *In Situ* ^{1}H NMR Irradiation Studies

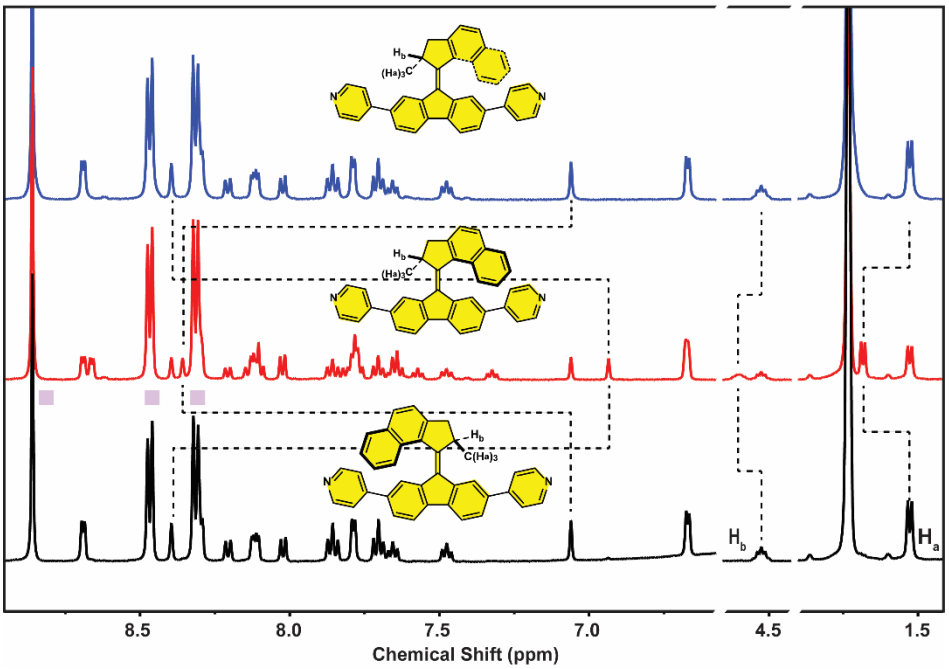

Figure S4 Comparison of ^{1}H NMR spectra (500 MHz, THF-d_8, -30 °C) of the PdTCPP and stable **1** (1:1) mixture (black spectrum), photostationary state mixture (red spectrum) and photostationary state mixture kept at the room temperature for 4 h in the dark (blue spectrum). The photostationary state ratio, established upon irradiation of the mixture of **PdTCPP** and **1** at 530 nm was determined by integration of the aliphatic (H_b) and aromatic (fluorene protons adjacent to the double bond) peaks.

5. SC-Xray Studies

Single-crystals were mounted on a cryoloop and placed in the nitrogen stream (100 K) of a Bruker-AXS D8 Venture diffractometer. Data collection and processing was carried out using the Bruker APEX3 software suite.[2] A multi-scan absorption correction was applied, based on the intensities of symmetry-related reflections measured at different angular settings (SADABS).[2] The structures were solved either using SHELXT[3] or SHELXS[4] and refinement was performed using SHELXL.[4] The hydrogen atoms were generated by geometrical considerations, constrained by idealized geometries and allowed to ride on their carrier atoms with an isotropic displacement parameter related to the equivalent displacement parameter of their carrier atoms. Contributions from disordered solvent present in structures of parent, motorized and interpenetrated **PdTCPP** MOFs as well as disordered pillars between the resolved porphyrin planes in parent and motorized **PdTCPP** MOFs were removed using the PLATON/SQUEEZE routine.[5]

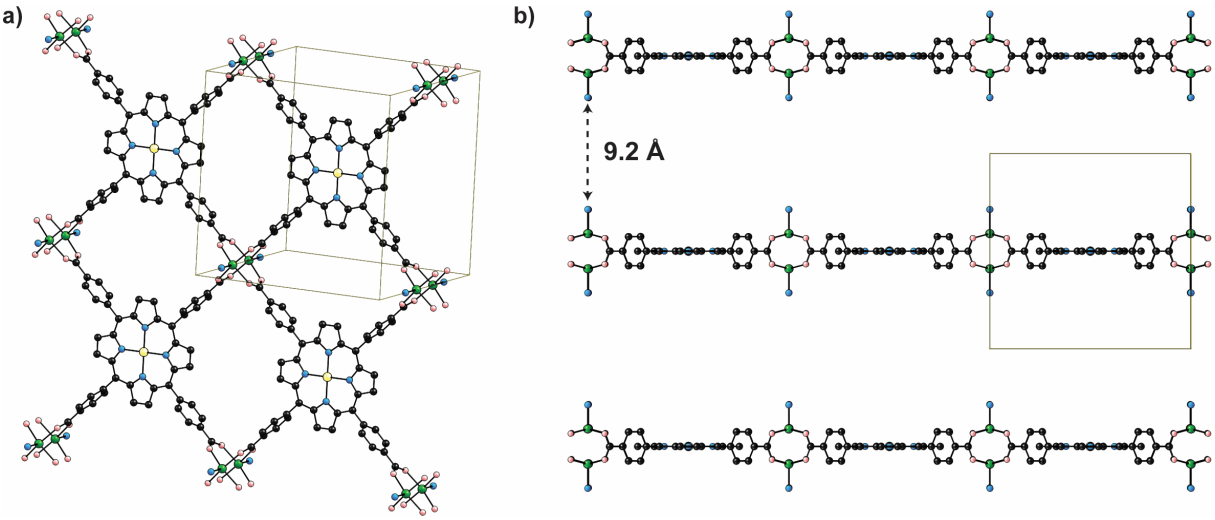

Figure S5 (**a**) Packing diagram of the two-dimensional layers of **PdTCPP** in the unit cell of the parent **PdTCPP-DPG** MOF. The elementary cell is marked with a yellow cuboid (a = 16.6421(8) Å, b = 16.6421(8) Å, c = 16.1146(15) Å). (**b**) Stacking of the two-dimensional layers in the c direction (black – carbon, blue – nitrogen, green – zinc, pink – oxygen, yellow – palladium).

CheckCIF Alerts:
THETM01_ALERT_3_A The value of sine(theta_max)/wavelength is less than 0.550: Calculated sin(theta_max)/wavelength = 0.5206
Severe disorder present in the structure led to a two-theta maximum of 107°. The data collection was appropriate for the sample and conditions, and it was possible to unambiguously establish the connectivity in the porphyrin planes as well as the distance between them.
PLAT242_ALERT_2_B Low MainMol Ueq as compared to neighbours of Zn1
Neighbouring porphyrin planes are connected via their Zn nodes giving the Zn centres less translational freedom compared to their neighbours.
PLAT250_ALERT_2_B Large U3/U1 Ratio for Average U(i,j) Tensor: 5.3
The rigidity of the porphyrins forming the layers of this structure leads to correlated thermal displacement along the pillar axis.

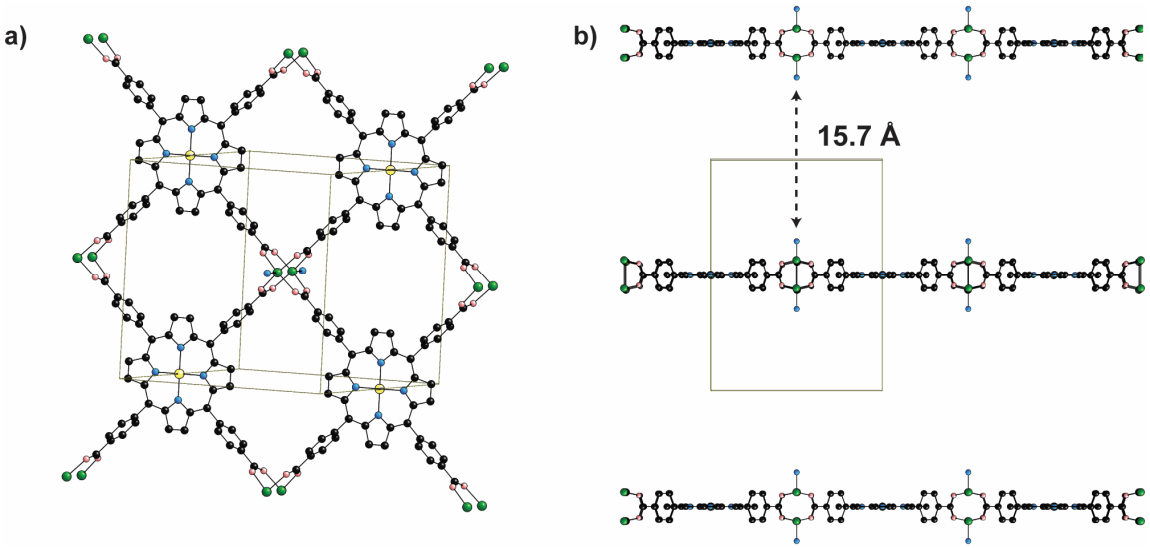

Figure S6 (**a**) Packing diagram of the two-dimensional layers of **PdTCPP** in the unit cell of the motorized **PdTCPP** MOF. The elementary cell is marked with a yellow cuboid (a = 16.625(3) Å, b = 16.625(3) Å, c = 22.463(8) Å). (**b**) Stacking of the two-dimensional layers in the c direction (black – carbon, blue – nitrogen, green – zinc, pink – oxygen, yellow – palladium).

CheckCIF Alerts:
THETM01_ALERT_3_A The value of sine(theta_max)/wavelength is less than 0.550: Calculated sin(theta_max)/wavelength = 0.4165
Severe disorder present in the structure led to a two-theta maximum of 80°. The data collection was appropriate for the sample and conditions, and it was possible to unambiguously establish the connectivity in the porphyrin planes as well as the distance between them.
RINTA01_ALERT_3_B The value of Rint is greater than 0.18: Rint given 0.239
PLAT020_ALERT_3_B The value of Rint is greater than 0.12: 0.239
Are caused by the weakly diffracting nature of these MOF crystals due to large amounts of disordered solvents and their poor quality.
PLAT084_ALERT_3_B High wR2 Value (i.e. > 0.25): 0.37
Resulting from weakly diffracting crystals and low quality of the obtained data.
PLAT213_ALERT_2_B Atom Pd1 has ADP max/min Ratio: 4.2 prolat
PLAT213_ALERT_2_B Atom C1 has ADP max/min Ratio: 4.2 prolat
PLAT213_ALERT_2_B Atom C4 has ADP max/min Ratio: 4.3 prolat
PLAT250_ALERT_2_B Large U3/U1 Ratio for Average U(i,j) Tensor: 7.3
Are caused by preferred thermal displacement along pillar axis in conjunction with poor data quality.
PLAT342_ALERT_3_B Low Bond Precision on C-C Bonds: 0.02667 Ang.
PLAT369_ALERT_2_B Long C(sp2)-C(sp2) Bond C3-C4: 1.58 Ang.
PLAT369_ALERT_2_B Long C(sp2)-C(sp2) Bond C7-C8: 1.61 Ang.
Are due to poor data quality.

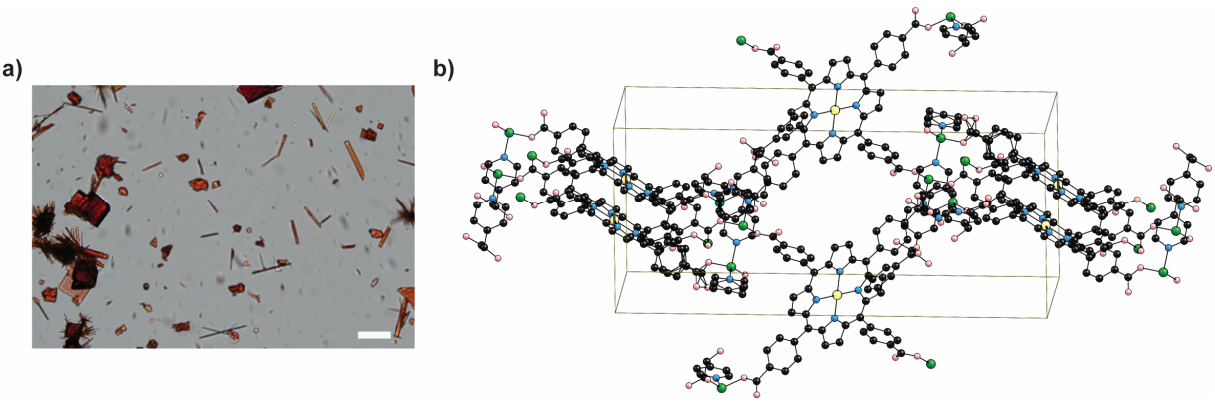

Figure S7 (**a**) Optical micrograph of the crystals obtained in solvothermal synthesis in a less acidic medium (see synthetic procedures section, scale bar100 μm). (**b**) Projection the along *c* direction of the SC-Xray structure of interpenetrated **PdTCPP-DPG** MOF forming needle-shaped crystals ($P2_1/n$ space group, hydrogens have been omitted for clarity, grey – carbon, light blue – nitrogen, dark grey – zinc, red – oxygen, turquoise – palladium).

CheckCIF Alerts:
THETM01_ALERT_3_A The value of sine(theta_max)/wavelength is less than 0.550: Calculated sin(theta_max)/wavelength = 0.4995
Severe disorder present in the structure led to a two-theta maximum of 101°. The data collection was appropriate for the sample and conditions, and it was possible to unambiguously establish the connectivity of the MOF structure.
PLAT420_ALERT_2_B D-H Without Acceptor: O5--H105
PLAT420_ALERT_2_B D-H Without Acceptor: O6--H106
Both groups, O5--H105 and O6--H106, are pointing into solvent filled voids in the 3D MOF structure. Hydrogen bonding is likely to occur with the disordered solvent molecules occupying these hollow spaces which were removed by PLATON/SQUEEZE.

Table S1 Crystallographic data of the synthesized MOFs

Nr.	LP-18017	LP-18030	LP-18039
Name	**PdTCPP-DPG**	Interpentrated MOF	Motorized **PdTCPP** MOF
Formula	$C_{48}H_{24}N_6O_8PdZn_2$	$C_{36}H_{24}N_4O_6Pd_{0.5}Zn$	$C_{12}H_6N_{1.5}O_2Pd_{0.25}Zn_{0.5}$
Molecular Weight	1049.87	727.16	262.47
Crystal System	tetragonal	monoclinic	tetragonal
T [K]	100(2)	100(2)	100(2)
Space Group	P4/mmm	P21/n	P 4/m m m
a [Å]	16.6421(8)	7.8815(11)	16.5927(19)
b [Å]	16.6421(8)	15.761(2)	16.5927(19)
c [Å]	16.1146(15)	33.580(5)	22.318(5)
α [°]	90	90	90
β [°]	90	93.750(4)	90
γ [°]	90	90	90
V [Å^3]	4463.1(6)	4162.5(10)	6144.7(19)
Z	1	4	4
D_{calc} [g·cm^{-3}]	0.391	1.160	0.284
F(0 0 0)	524	1476	524
h_{min}, h_{max}	–17, 17	–7, 7	–13, 13
k_{min}, k_{max}	–17, 17	–12, 15	–13, 13
l_{min}, l_{max}	–16, 16	–31, 33	–18, 18
μ [mm^{-1}]	1.245	2.850	0.905
Crystal Size [mm]	0.25 x 0.20 x 0.08	0.19 x 0.06 x 0.03	0.20 x 0.20 x 0.06
Colour, Shape	clear_dark_red plate	clear_dark_red needle	clear_dark_red plate
R_{int}	0.1790	0.1078	0.2393
θ_{min}, θ_{max} [°]	3.756, 53.386	2.637, 50.368	2.663, 39.958
Total Reflections (before merge)	33559	16837	67241
Data (I>3 x sigma(I)) [Reflections,Parameters,Restraints]	1588, 59, 12	4320, 533, 1246	1149, 59, 139
S (=GooF)	1.060	1.040	1.052
Min. Residual Density [e/Å^3]	–0.669	–0.858	–0.656
Max. Residual Density [e/Å3]	1.601	0.368	1.369
Threshold Expression	I>2sigma(I)	I>2sigma(I)	I>2sigma(I)
R_1	0.0747	0.0917	0.1590
wR_2	0.1850	0.1251	0.3715

6. PXRD Studies

a. Experimental PXRD

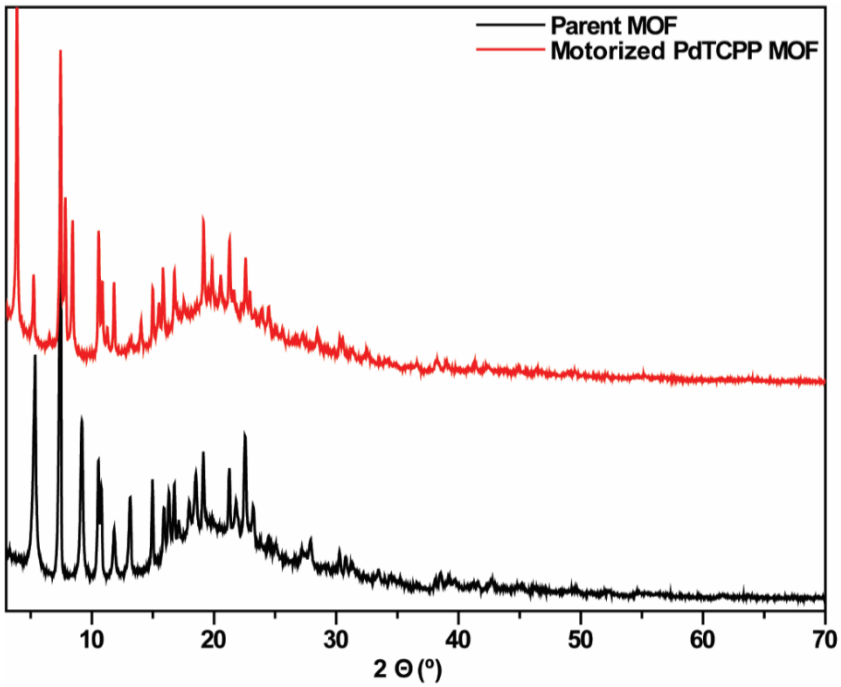

Figure S8 PXRD patterns of **PdTCPP-DPG** (black line) and motorized **PdTCPP** (red line) MOFs.

b. Pawley Refinement of PXRD Data

Pawley refinement of powder X-ray diffraction (PXRD) patterns and establishment of structural models were performed using Materials studio Software suite.[6] Indexing of the PXRD patterns of both MOFs showed best agreement for a tetragonal symmetry with space group P4/mmm. This is in agreement with the single crystal diffraction experiments for which a partial crystal structure of **PdTCPP-DPG** could be obtained.

For **PdTCPP-DPG** MOF a tetragonal unit cell with lattice parameters $a = b = 16.76176(6)$ Å, $c = 16.34245(1)$ Å. This is in good agreement with the original single crystal data on **PdTCPP-DPG** MOF with a unit cell in space group P4/mmm and lattice parameter $a = b = 16.97084(8)$ Å, $c = 16.1146(15)$ Å which was collected at 100 K in contrast to the PXRD data which was recorded at ambient temperature. For motorized **PdTCPP** MOF a tetragonal unit cell with lattice parameter $a = b = 16.76049(8)$ Å, $c = 22.50124(1)$ Å could be refined from PXRD data. This represents an elongation of the unit cell in the *c*-direction of 38% proportional to the elongation of the pillaring ligand while *a*, *b* lattice constants are found to be almost identical to **PdTCPP-DPG** MOF. The parameters for Pawley refinement are summarized in Table S1. Due to the high degree of disorder in the ligand backbone and the presence of solvent in the pores which could not be removed under preservation of the framework attempts to perform Rietveld refinement of the MOF structures based on the PXRD data were unsuccessful.

Table S2 Parameters for Pawley refinement of **PdTCPP-DPG** and motorized **PdTCPP** MOFs

	PdTCPP-DPG MOF	motorized **PdTCPP** MOF
Symmetry, space group	Tetragonal, *P4/mmm*	Tetragonal, *P4/mmm*
Unit cell parameter, (Å)	*a* = *b* =16.97084(8) Å, c = 16.1146(15) Å	*a* = *b* = 16.76049(8) Å, *c* = 22.50124(1) Å
Unit cell volume, (Å^3)	4641.15(4)	6320.91(5)
Wave length (Å)	1.5406	
2θ range (°)	3–70	
Instrument geometry	Debye-Scherrer	
Profile function	Pseudo-Voigt	
U	1.10545	0.38304
V	–0.20962	–0.09926
W	0.02488	0.03223
N_A	0.93327	0.57046
N_B	0.00095	0.00363
Line shift	Debye-Scherrer	
Shift #1	–0.07229	–0.10382
Shift #2	0.43367	0.41353
Final R_{wp}	0.0409	0.071
Final R_p	0.03	0.0414
R_{wp} (without background)	0.0542	0.162

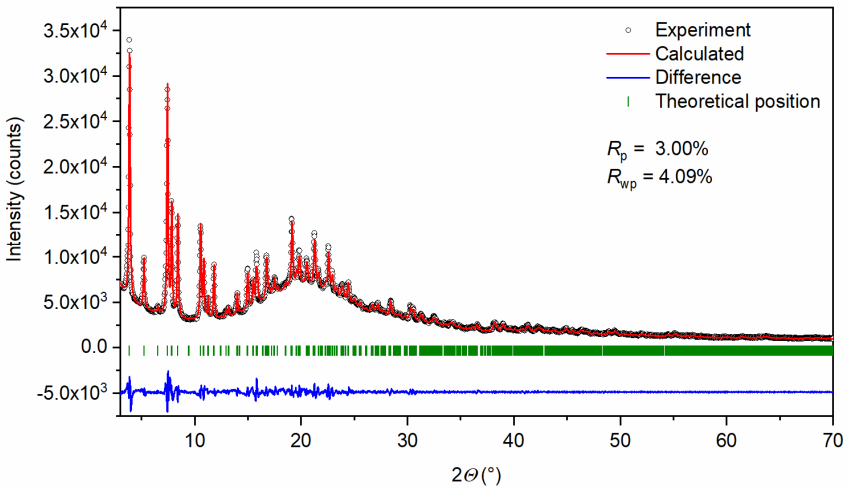

Figure S9 PXRD pattern (empty circles) and Pawley refinement (red line) of the **PdTCPP-DPG** pillared paddlewheel MOF. The difference plot (blue) and Bragg peak positions (green) are provided.

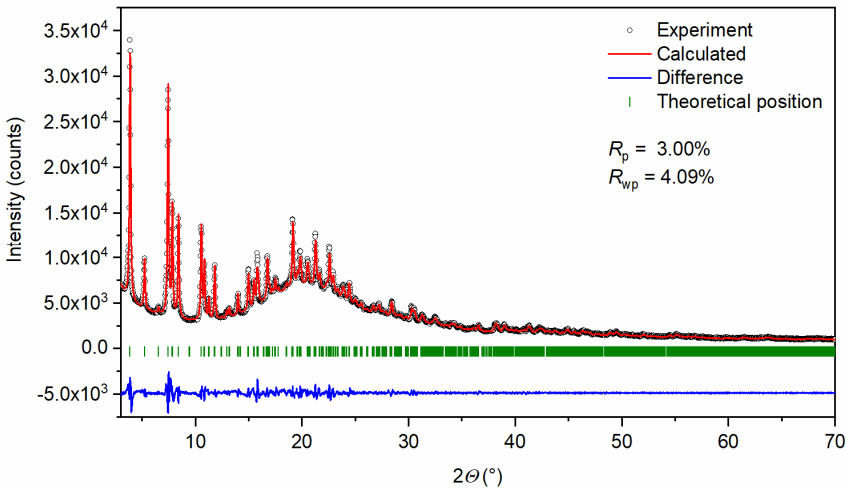

Figure S10 PXRD pattern (empty circles) and Pawley refinement (red line) of the motorized **PdTCPP** pillared paddlewheel MOF. The difference plot (blue) and Bragg peak positions (green) are provided.

Based on the refined unit cell parameter and the partial single crystal structure of **PdTCPP-DPG** MOF, structural models for both MOFs were established. Due to the asymmetry of the pillaring ligand molecules the symmetry of the unit cell was reduced from *P*4/*mmm* to triclinic, $\boldsymbol{P\bar{1}}$ and ***P*1** for **PdTCPP-DPG** and motorized **PdTCPP** MOFs, respectively. To maintain the tetragonal symmetry of the unit cell, angles were kept constrained to 90° and *a* and *b* were kept identical. For structural modelling of the pillaring ligands the DFT optimized structures of **DPG** and molecular motor **1** were introduced between the Zn-porphyrin layers (obtained from the single crystal structure of **PdTCPP-DPG** MOF) and connected to the axial open metal sites of the Zn-paddle wheel nodes. Geometrical optimization was performed using the forcite module and universal force field implemented in Material Studio. To avoid changes in the molecular structure of the Zn-porphyrin layers constraints were applied on these groups and only molecular positions of the pillars were optimized. A similar constraint was applied on the structure of the motor to maintain the geometry of the DFT optimized structure (Figure S11).

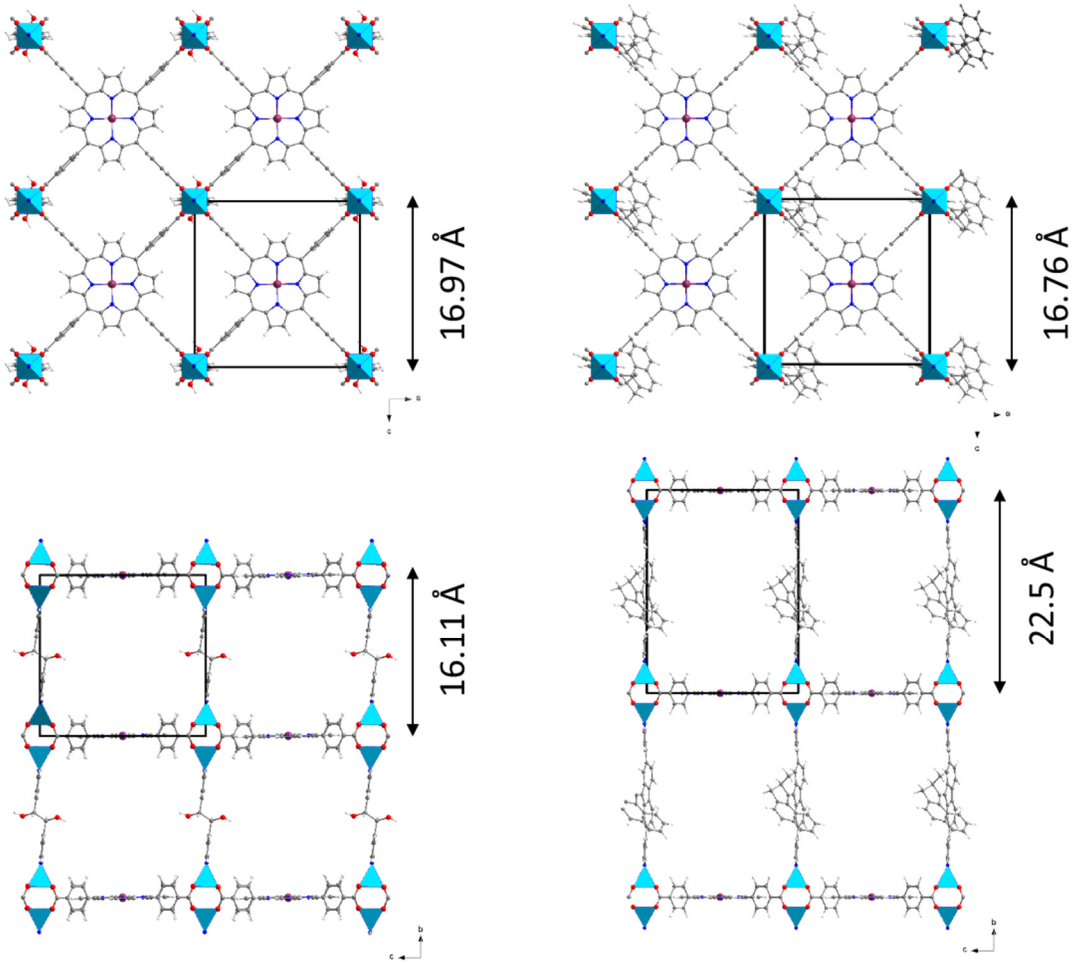

Figure S11 Structural models of parent **PdTCPP-DPG** MOF (left top and bottom panel) and motrized **PdTCPP** MOF (right top and bottom panels)

7. UV/Vis Studies of the Sensitized Photochemical Isomerization and Thermal Helix Inversion of the Molecular Motor

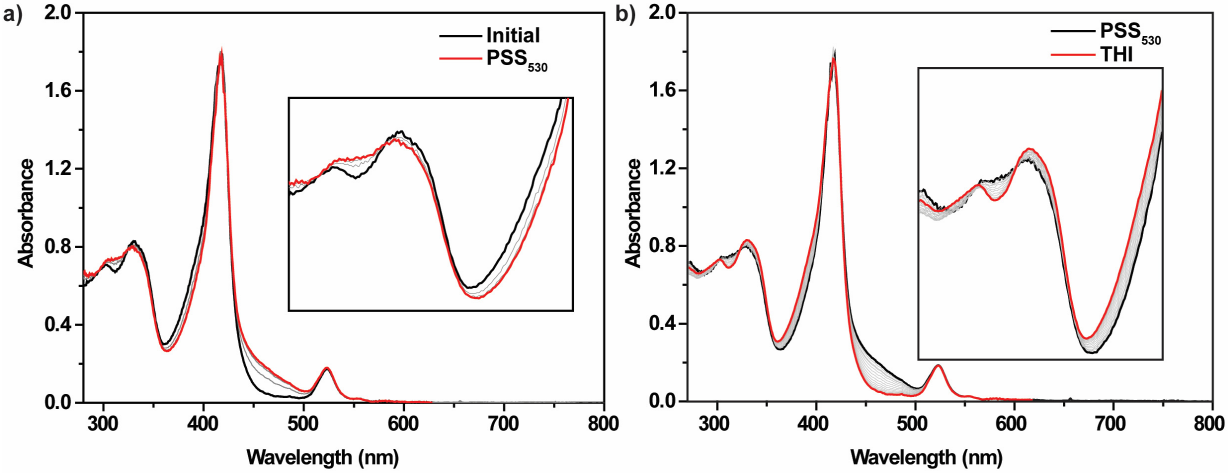

Figure S12 Example of characteristic changes in the UV/Vis spectrum of equimolar **PdTCPP** and molecular motor **1** mixture upon irradiation at 530 nm (black line – initial spectrum, red line – final spectrum) and during thermal helix inversion (black line – initial spectrum, red line – final spectrum) both recorded at 10 °C for same sample. Grey lines indicate intermediate states recorded every 90 s. Presence of an isosbestic point at 323 nm indicates that both processes are unimolecular. Insets show expansion of the region between 230 – 400 nm.

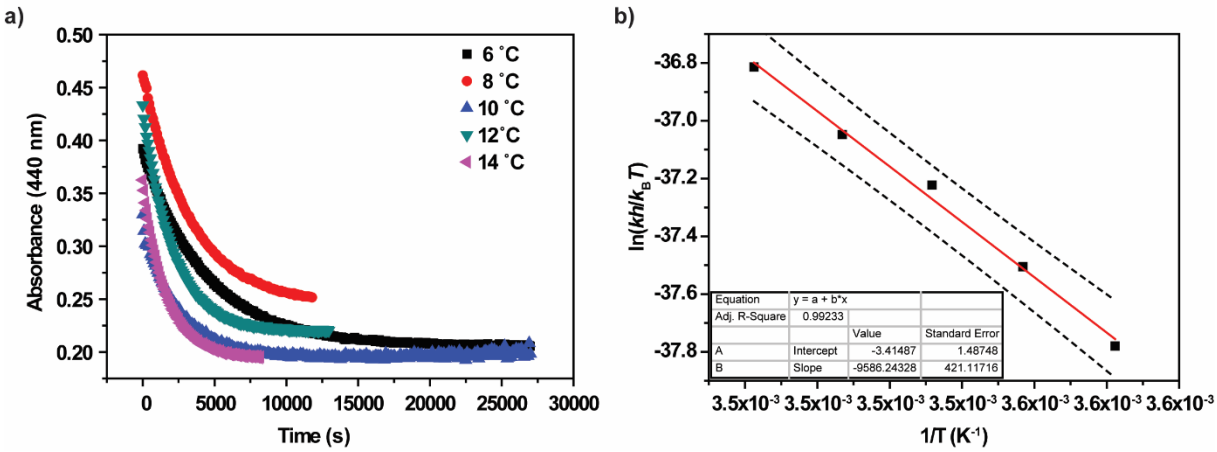

Figure S13 (**a**) Changes in absorbance at 440 nm during thermal helix inversion of the metastable 1 isomer in mixture of **PdTCPP** and **1** (1:1) in DMF followed in range of temperatures (6-14 °C) over time with UV/Vis absorption spectroscopy. (**b**) Eyring plot analysis of the thermal helix inversion of the metastable isomer of **1** generated by energy transfer from PdTCPP in DMF. Thermodynamic parameters were obtained by fitting to the linearized form of Eyring equation using Origin software. Dashed lines indicate 95% confidence interval.

8. Energy transfer in Solution

a. Phosphorescence Intensity and Stern-Volmer Plot

Figure S14 (a) Comparison of steady-state emission spectra (λ_{exc} = 530 nm) of **PdTCPP** (44.6 µM, DMF) and mixtures of **PdTCPP** and **1** of va

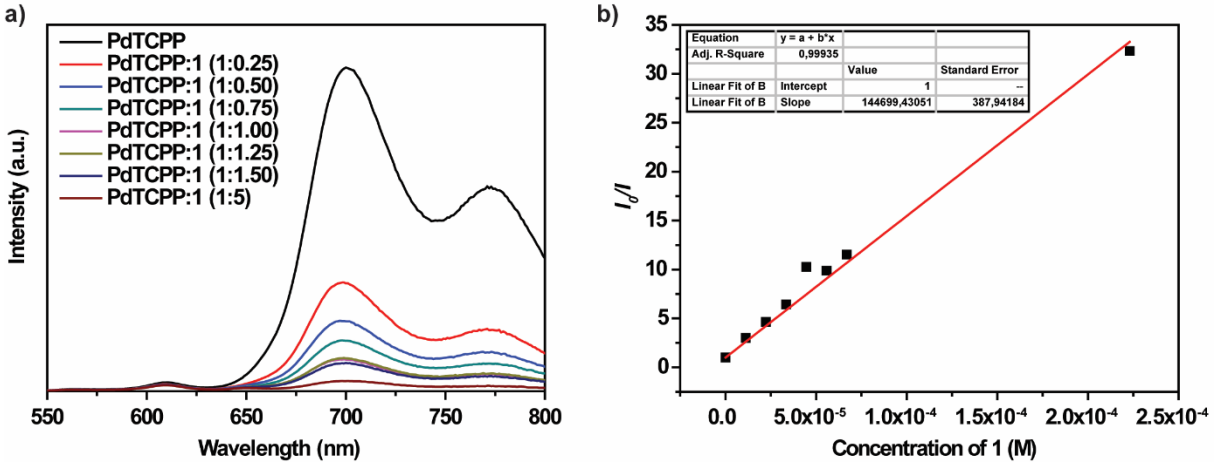

rious ratios. **(b)** Corresponding Stern-Volmer plot obtained from intenisites at 700 nm.

b. Phosphorescence Lifetimes and Stern-Volmer Plot

Emission decays curves in solution were recorded using a pulsed microsecond Xenon flash lamp (5 W) and measured within at least five lifetime long time window. After each measurement the instrument response functions (IRF) were recorded using scattering of LUDOX® colloid. The emission decay curves were deconvoluted by reconvolution of IRF and a minimal number of exponential decay functions to give a small χ^2 values and random residual plots using an analysis routine implemented in the software provided by the manufacturer of the equipment. Systematic patterns in the residuals were detected only in the initial part of the emission decay curves for samples with higher molecular motor **1** concentrations and were assumed to originate from the imperfection of IRF acquisition.

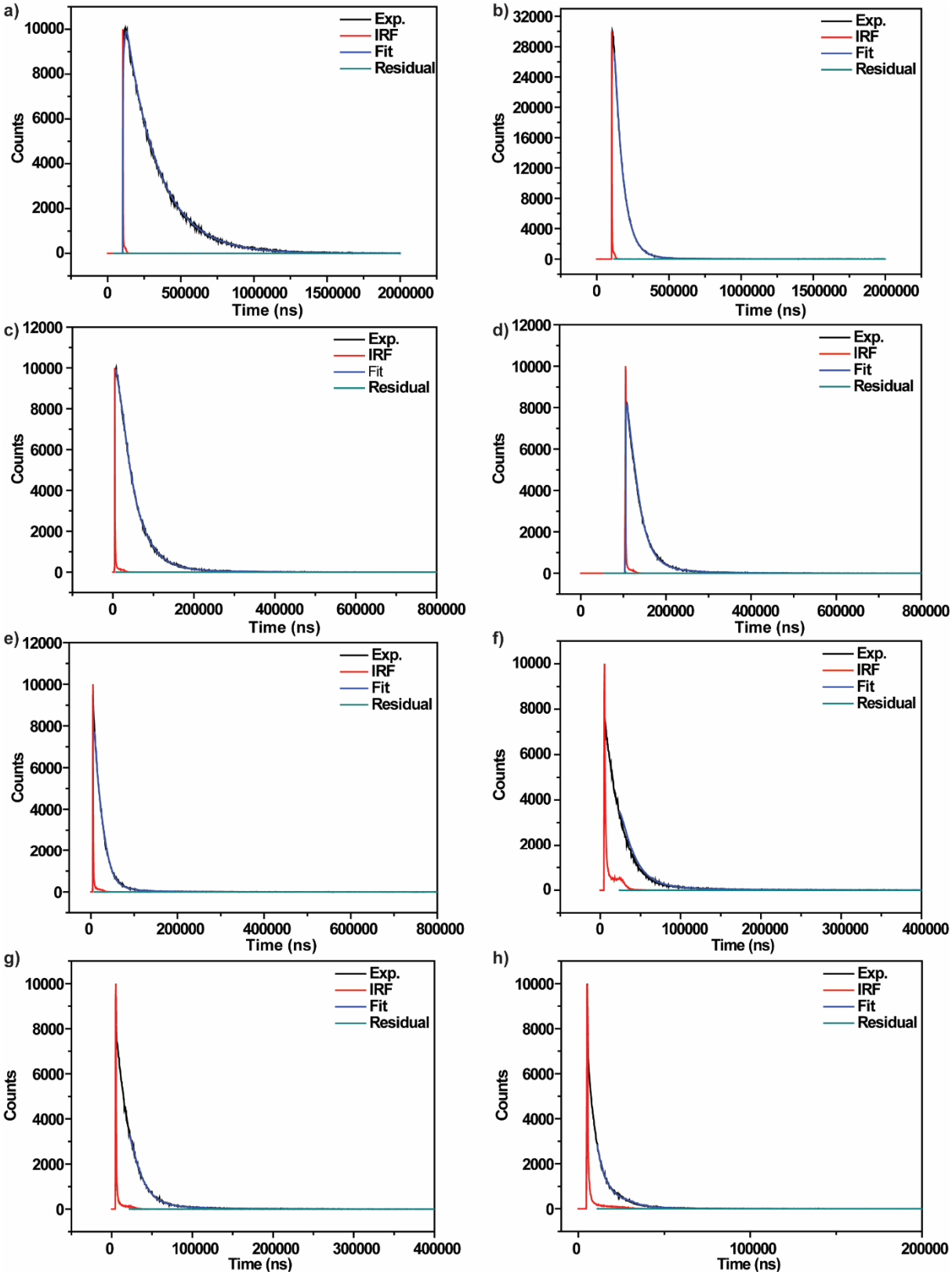

Figure S15 Comparison of the recorded emission decay curves of **PdTCPP** (44.6 μM, DMF, λ_{exc} = 530 nm) (a) and **PdTCPP**:**1** mixtures (in DMF, concentration of PdTCPP was kept 44.6 μM) with increasing conctntration of molecular motor **1**, (**b**) – 11.2 μM (0.25 eqiv.), (**c**) – 22.3 μM (0.50 eqiv.), (**d**) – 33.5 μM (0.75 eqiv.), (**e**) – 44.6 μM (1.00 eqiv.), (**f**) – 55.8 μM (1.25 eqiv.), (**g**) – 67.2 μM (1.50 eqiv.), (**h**) – 223 μM (5.00 eqiv.). Black line shows the recorded decay, red an IRF function, blue result of the fitting and green residual plot.

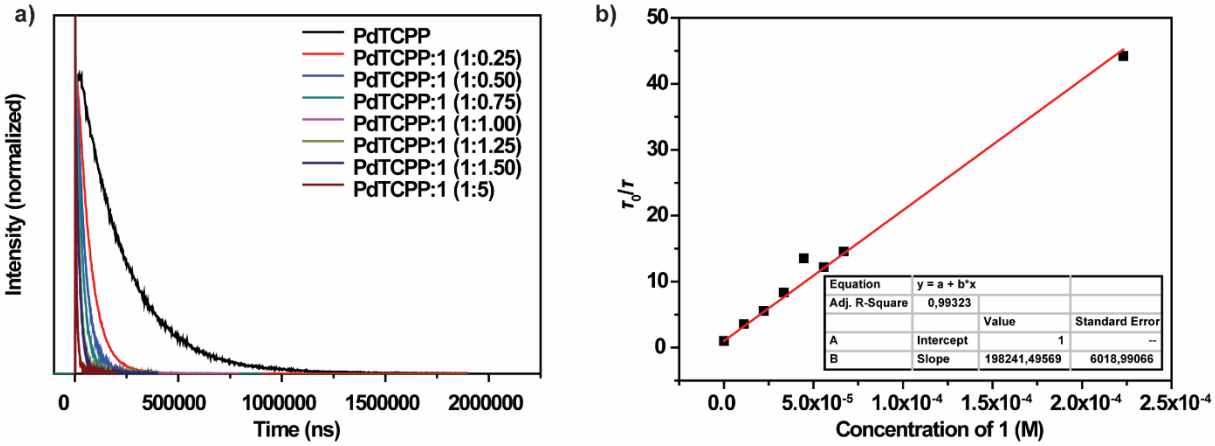

Figure S16 (**a**) Comparison of the normalized emission decays curves for mixtures of **PdTCPP** and **1** with varying concentration of molecular motor **1**. (**b**) Corresponding Stern-Volmer plot of phosphorescence quenching.

9. Quantum Yields

Quantum yields of phosphorescence were determined in an integrating sphere with a cuvettes oriented at an oblique angle to the beam path. Liquid samples were kept in a tightly sealed cuvettes equipped with a black screw-cap tightly sealed with septa. Quantum yields were computed using an analysis routine implemented in the software provided by the manufacturer of the equipment by comparison of the area of the phosphorescence emission band to the amount of the absorbed photons. The amount of the absorbed photons was derived from attenuation of the Rayleigh scattering peak in comparison to the scattering of the pure solvent sample measured with exactly same experimental parameters and solvent volume. Additionally quantum yield of phosphorescence of the solution of pure **PdTCPP** was measured in a cuvette capped with a white cap directly after removal of the sample from a glove box, which provided a scaling factor for quantum yields for all the samples to compensate for the absorption by the black screw-cap. All the relevant photo-physical parameters are shown in **Table S3**.

Table S3 Comparison of the photo-physical data in solution.

PdTCPP:**1**	1:0	1:0.25	1:0.50	1:0.75	1:1.00	1:1.25	1:1.50	1:5.00
τ_1/μs	220.9±0.2	60.3±0.1	37,6±0.2	23.4±0.1	14.8±0.1	16.2±0.2	13.8±0.1	4.5±0.1
τ_2/μs	-	216±4	107±3	94.3±1.2	63.8±1.1	75±2	61.1±1.2	27.8±0.6
τ_{avg}/μs	-	62.0±0.2	39.9±0.3	26.4±0.16	16.3±0.1	18.1±0.2	15.2±0.2	5.01±0.1
χ^2	0.000489	1.3363	1.0948	0.00176	1.2748	4.5197	1,1641	1.1862
$\Phi_{Phoshor}$/%	5.6	1.8	1.2	0.82	0.52	0.54	0.46	0.17

errors were derived from the fit;

10. Energy Transfer in the Solid State

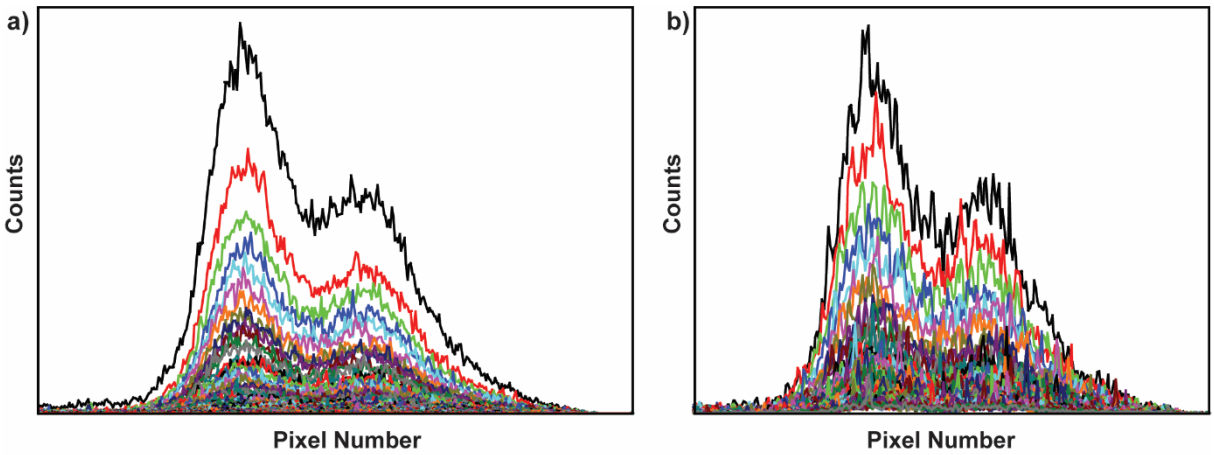

Figure S17 (**a**) Time dependent emission spectra of **PdTCPP-DPG** MOF sample. Spectra were measured every 10 µs. (**b**) Time dependent emission spectra of motorized **PdTCPP** MOF sample. Spectra were measured every 500 ns (each two subsequent spectra were averaged for clarity).

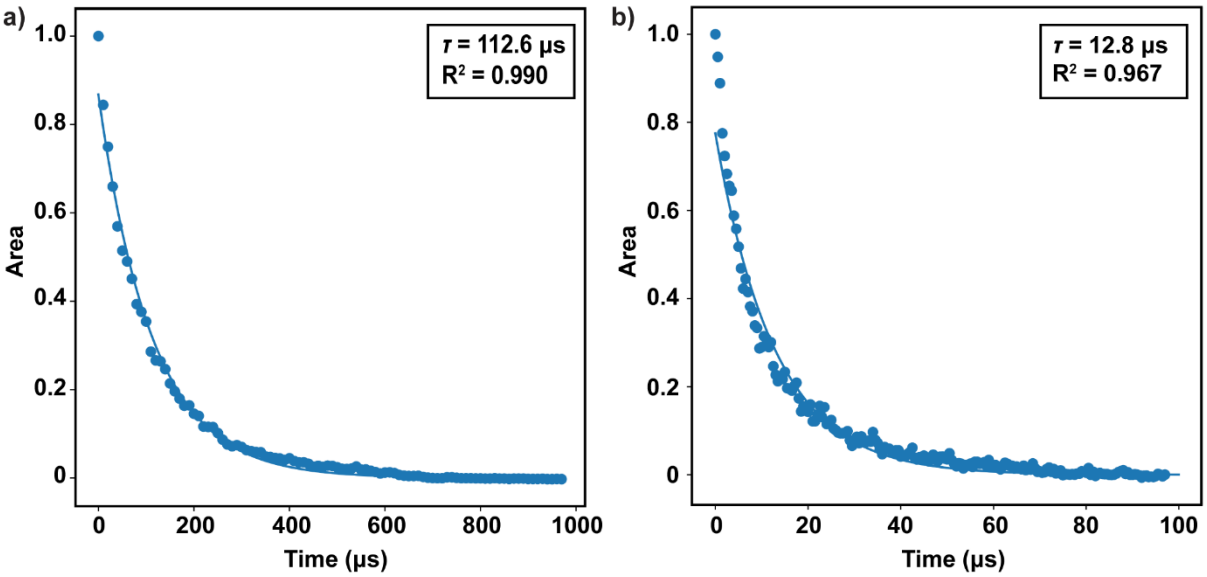

Figure S18 (**a**) Changes in the area of the phosphorescence band of the **PdTCPP-DPG** MOF (blue dots) and results of the monoexponential fitting (blue line). (**b**) Changes in the area of the phosphorescence band of the motorized **PdTCPP** MOF (blue dots) and results of the monoexponential fitting (blue line). Lifetimes and goodness of the fits are given in the box.

11. Photochemical and Thermal Isomerization Studies in the Solid State

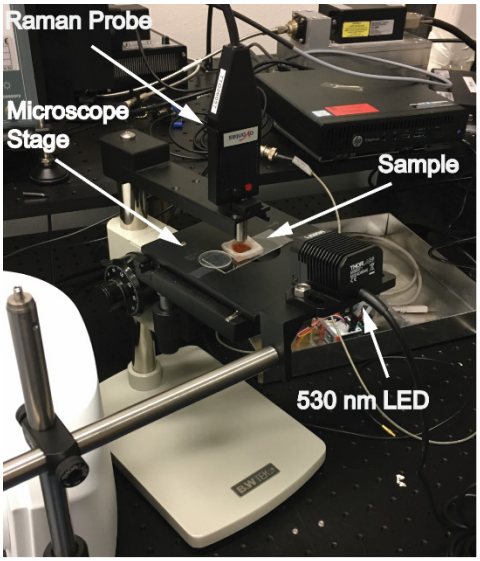

Figure S19 Photograph of the experimental setup used for Raman studies in the solid state.

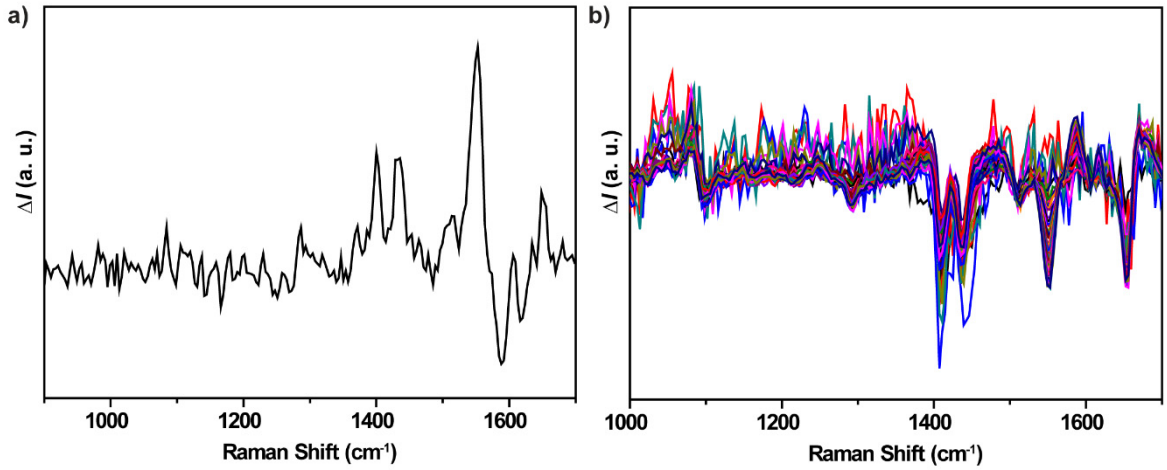

Figure S20 Difference Raman spectra (1064 nm, 250 mW) of the DMF solution of **PdTCPP** and **1** (1:1) ratio during irradiation at 530 nm at -20 °C (**a**) and subsequent thermal helix inversion (**b**). Spectra were obtained by subtraction of the initial spectrum from the following spectra. Note that subtraction for bands characteristic of DMF (ca. 1400 cm^{-1}) was imperfect.

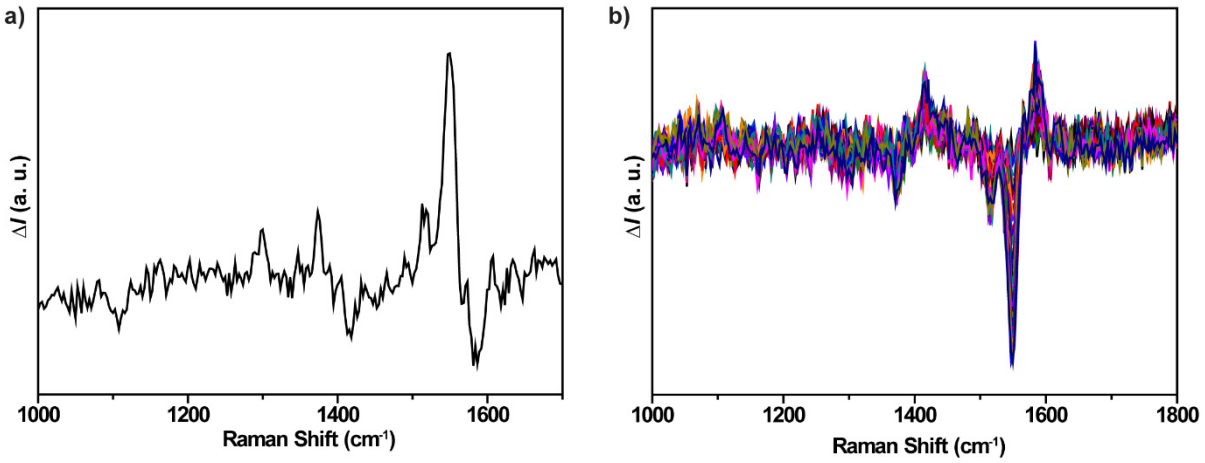

Figure S21 Difference Raman spectra (1064 nm, 250 mW) of motorized **PdTCPP** MOF during irradiation at 530 nm (**a**) and subsequent thermal helix inversion (**b**). Spectra were obtained by subtraction of the initial spectrum from the following spectra.

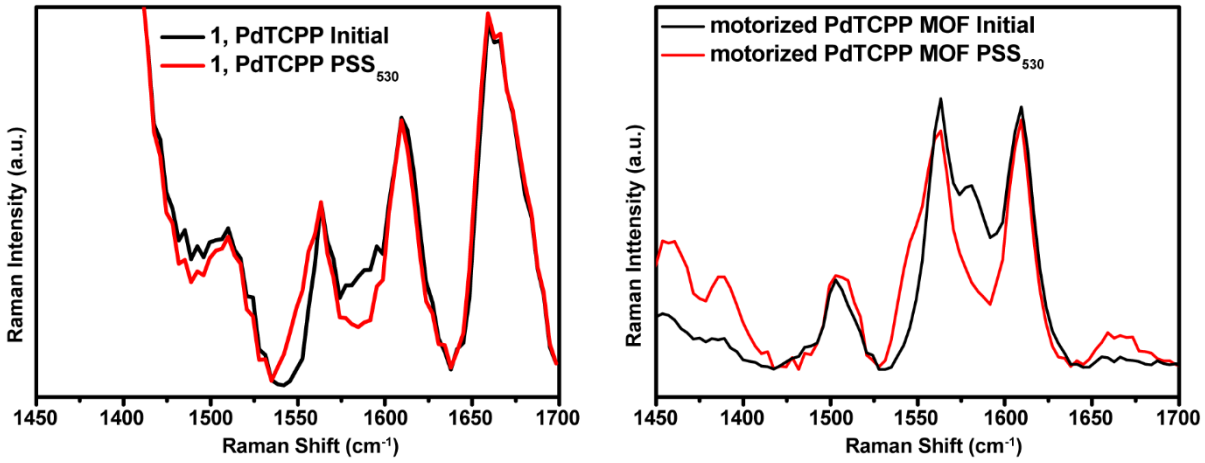

Figure S22 Comparison of PSS_{530} Raman spectra (1064 nm, 250 mW, red lines) of **PdTCPP**:**1** mixture at -20 °Cin DMF (left) and motorized **PdTCPP** MOF (right). Ratios of scattering intensities for bands characteristic of metastable and stable isomer of **1** (I_{1581}/I_{1550}) of 1.2 and 1.6 for solution and solid, respectively, indicates that the composition of PSS mixture is similar in both cases.

a. Variable Power Raman Experiments

Rate of the thermal helix inversion of the metastable isomer of molecular motor struts in motorized **PdTCPP** MOF was followed over time with 1064 nm Raman spectroscopy. Spectra were processed with adaptive baseline using Spectragryph software. It was found that the rate of thermal helix inversion of metastable-**1** follows first-order kinetics and rate constants for this process were calculated by fitting the changes in the Raman intensity (1530 – 1560 cm^{-1} spectral region) to the linearized equation:

$$\ln\frac{I - I_\infty}{I_0 - I_\infty} = -kt$$

where, I is Raman intensity at particular Raman shift, I_0 is scattering intensity directly after irradiation at 530 nm was discontinued and I_∞ is intensity for the stable isomer (Figure S23). Gibbs free energy of activation of the helix inversion was calculated from the obtained rate constants using Eyring equation. In addition, variable power Raman experiments (Figures S24, S25) showed that the activation barrier of the helix inversion of **1** is independent on the laser power (Table S4) thus excluding the influence of the local heating on the rate of the thermal process.

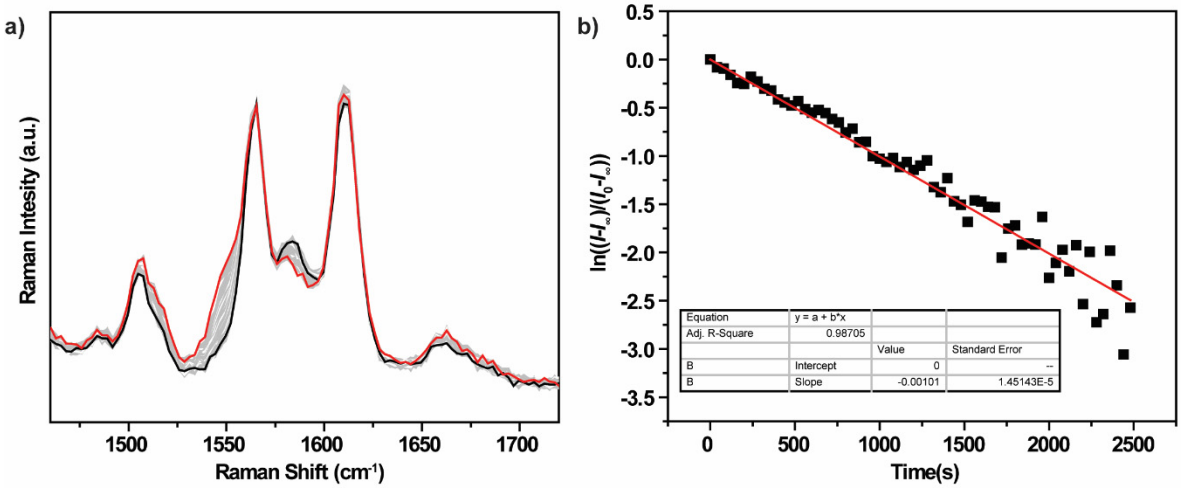

Figure S23 (**a**)Example of the changes in the Raman spectrum (250 mW, 40 s integration time) of the motorized **PdTCPP** MOF during thermal helix inversion. (**b**) Kinetic plot constructed by following the changes in Raman intensity at 1552 cm^{-1}.

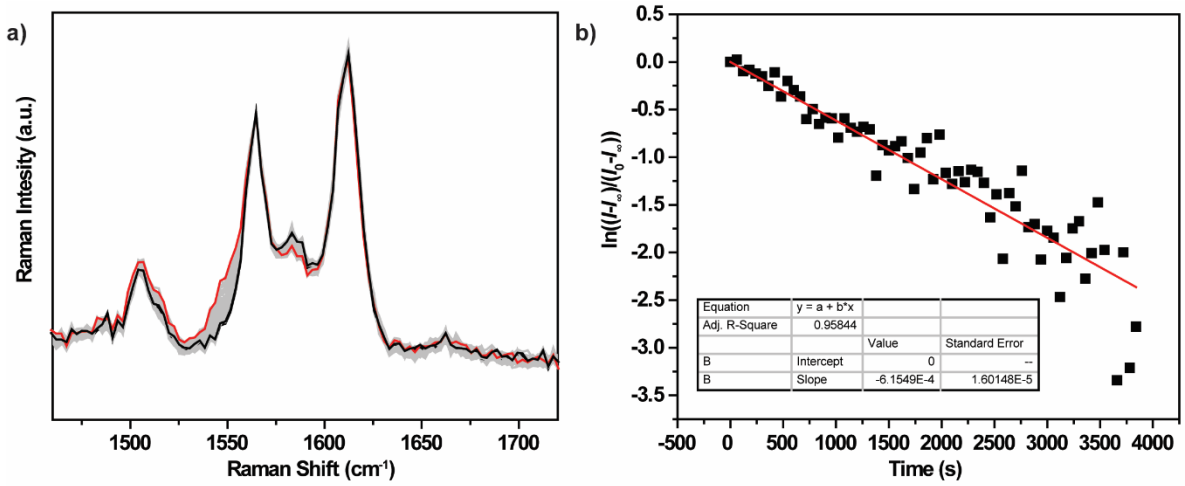

Figure S24 (**a**)Example of the changes in the Raman spectrum (~150 mW, 60 s integration time) of the motorized **PdTCPP** MOF during thermal helix inversion. (**b**) Kinetic plot constructed by following the changes in Raman intensity at 1548 cm^{-1}.

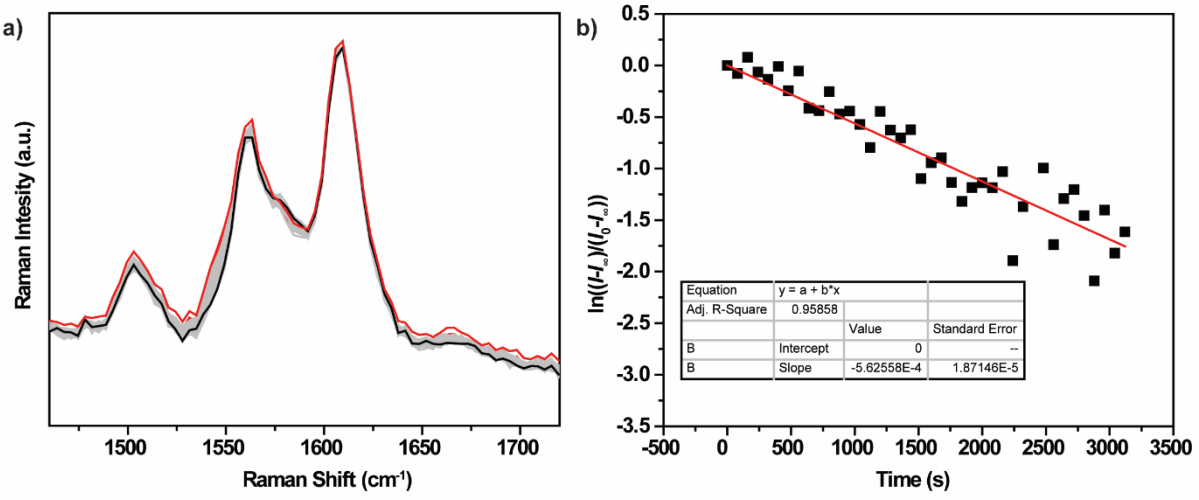

Figure S25 (**a**)Example of the changes in the Raman spectrum (~70 mW, 80 s integration time) of the motorized **PdTCPP** MOF during thermal helix inversion. (**b**) Kinetic plot constructed by following the changes in Raman intensity at 1556 cm^{-1}.

Table S4 Observed Gibbs free energy values for thermal-helix inversion of metastable isomer 1 in motorized PdTCPP MOF

Transmitted Laser Power*	$\Delta^{\ddagger}G$(20 °C) /kJ·mol^{-1}
250 mW	88.7±0.8
150 mW	89.3±1.2
70 mW	89.1±1.4

*Approximated transmitted laser power was measured using a FieldMate laser power meter (RoHS compliant)

12. Other Spectra

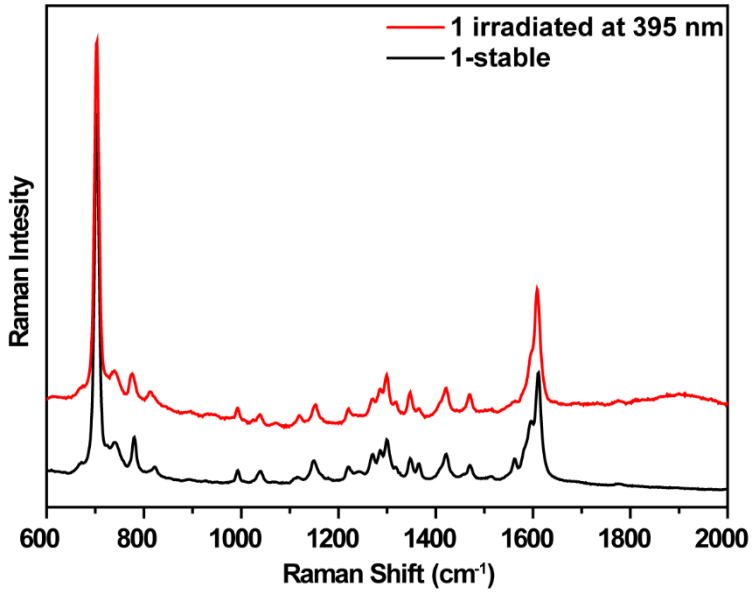

Figure S26 Comparison of resonance Raman spectra (355 nm) in DCM of **1**-stable (black spectrum) and **1** irradiated at 395 nm to generate the metastable isomer.

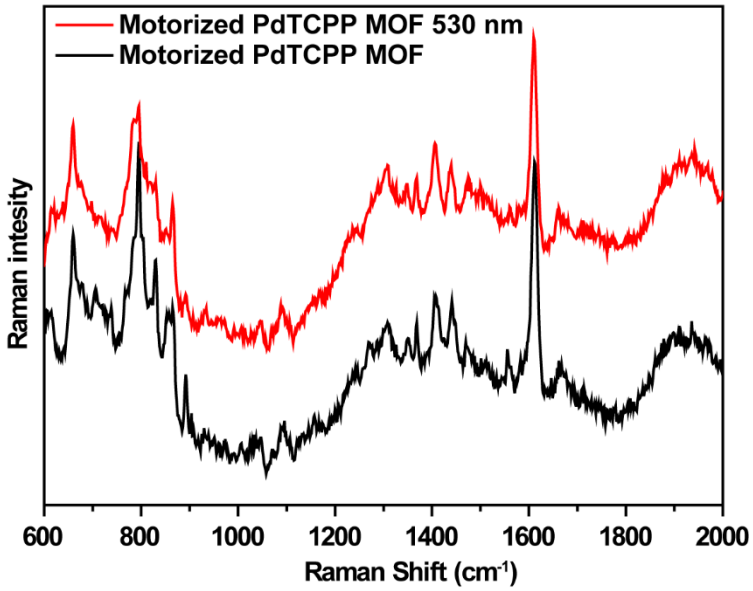

Figure S27 Comparison of resonance Raman spectra (355 nm) of motorized **PdTCPP** MOF pristine (black spectrum) and irradiated at 530 nm (red spectrum) with fast rastering of the sample stage. It should be noted that attempts to record resonance Raman spectra of **PdTCPP** MOFs without rastering was obstructed by strong fluorescence background and burning of the solid samples.

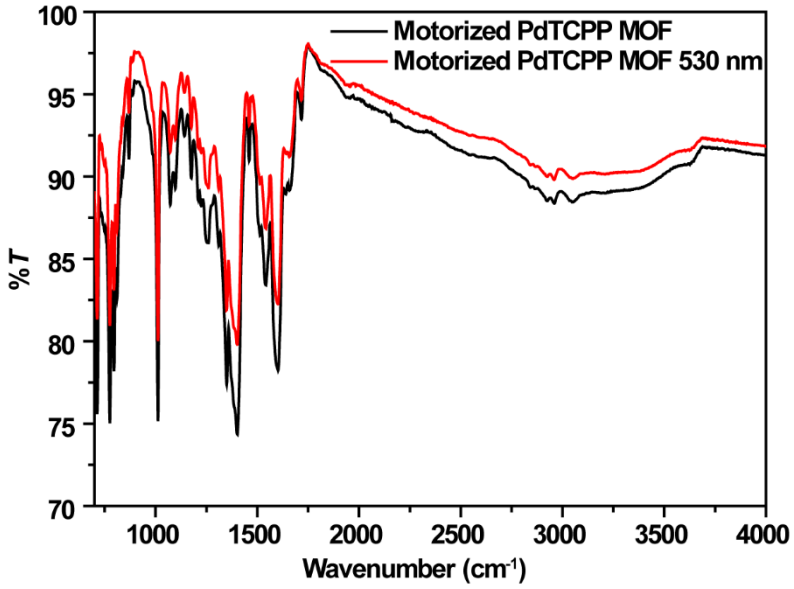

Figure S28 Comparison of FTIR-ATR spectra of motorized **PdTCPP** MOFs pristine (black spectrum) and irradiated at 530 nm (red spectrum).

13. Computational Details

Density functional theory (DFT) calculations were carried out with the Gaussian 09 program (rev. D.01).[7] All of the calculations were performed on systems in the gas phase using the Becke's three-parameter hybrid functional[8] with the LYP correlation functional[9,10] (DFT B3LYP/6-31G(d,p)). Each geometry optimization was followed by a vibrational analysis to determine that it represents a minimum on the potential energy surface.

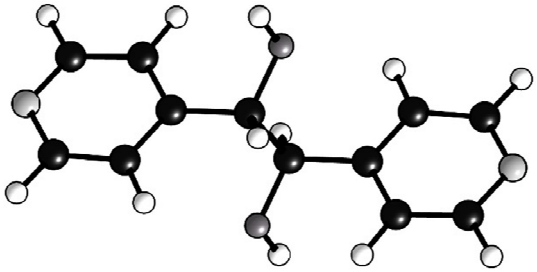

Number of imaginary frequencies: 0

SCF Energy (B3LYP/6-31G(d,p)): -724.4460106

C	0.943613000	-0.343709000	-4.033003000
C	1.120532000	-0.109159000	-2.668992000
C	0.037471000	0.352434000	-1.915475000
C	-1.174151000	0.554283000	-2.582302000
C	-1.245059000	0.288806000	-3.949084000
H	1.776477000	-0.701140000	-4.636376000
H	2.084407000	-0.272230000	-2.198540000
H	-2.049756000	0.905215000	-2.045879000
H	-2.179681000	0.441696000	-4.485757000
C	0.181477000	0.621149000	-0.426383000
H	-0.518332000	1.420139000	-0.137536000
C	-0.181477000	-0.621149000	0.426383000
H	0.518332000	-1.420139000	0.137536000
C	-0.037471000	-0.352434000	1.915475000
C	-1.120532000	0.109159000	2.668992000
C	1.174151000	-0.554283000	2.582302000
C	-0.943613000	0.343709000	4.033003000
H	-2.084407000	0.272230000	2.198540000
C	1.245059000	-0.288806000	3.949084000
H	2.049756000	-0.905215000	2.045879000
H	-1.776477000	0.701140000	4.636376000
H	2.179681000	-0.441696000	4.485757000
O	-1.515330000	-0.954884000	0.070814000
H	-1.759638000	-1.756783000	0.551172000
O	1.515330000	0.954884000	-0.070814000
H	1.759638000	1.756783000	-0.551172000
N	-0.212245000	-0.152307000	-4.680175000
N	0.212245000	0.152307000	4.680175000

14. References

(1) Danowski, W.; van Leeuwen, T.; Abdolahzadeh, S.; Roke, D.; Browne, W. R.; Wezenberg, S. J.; Feringa, B. L. Unidirectional Rotary Motion in a Metal–organic Framework. *Nat. Nanotechnol.* 2019, *14* (5), 488–494.

(2) Bruker, (2016). APEX3 (V2016.1-0), SAINT (Version 8.37A) and SADABS (Version 2014/5). Bruker AXS Inc., Madison, Wisconsin, USA.

(3) Sheldrick, G. M. SHELXT - Integrated Space-Group and Crystal-Structure Determination. *Acta Crystallogr. Sect. A Found. Crystallogr.* 2015, *71* (1), 3–8.

(4) Sheldrick, G. M. A Short History of SHELX. *Acta Crystallographica Section A: Foundations of Crystallography*. International Union of Crystallography January 1, 2008, pp 112–122.

(5) Spek, A. L. PLATON SQUEEZE: A Tool for the Calculation of the Disordered Solvent Contribution to the Calculated Structure Factors. *Acta Crystallogr. Sect. C Struct. Chem.* 2015, *71* (1), 9–18.

(6) BIOVIA Materials Studio 2017; Dassault Systèmes, Waltham, MA, 2016.

(7) Frisch, M. J.; Trucks, G. W.; Schlegel, H. B.; Scuseria, G. E.; Robb, M. A.; Cheeseman, J. R.; Scalmani, G.; Barone, V.; Mennucci, B.; Petersson, G. A.; Nakatsuji, H.; Caricato, M.; Li, X.; Hratchian, H. P.; Izmaylov, A. F.; Bloino, J.; Zheng, G.; Sonnenberg, J. L.; Hada, M.; Ehara, M.; Toyota, K.; Fukuda, R.; Hasegawa, J.; Ishida, M.; Nakajima, T.; Honda, Y.; Kitao, O.; Nakai, H.; Vreven, T.; Montgomery, J. A., Jr.; Peralta, J. E.; Ogliaro, F.; Bearpark, M.; Heyd, J. J.; Brothers, E.; Kudin, K. N.;

Staroverov, V. N.; Kobayashi, R.; Normand, J.; Raghavachari, K.; Rendell, A.; Burant, J. C.; Iyengar, S. S.; Tomasi, J.; Cossi, M.; Rega, N.; Millam, N. J.; Klene, M.; Knox, J. E.; Cross, J. B.; Bakken, V.; Adamo, C.; Jaramillo, J.; Gomperts, R.; Stratmann, R. E.; Yazyev, O.; Austin, A. J.; Cammi, R.; Pomelli, C.; Ochterski, J. W.; Martin, R. L.; Morokuma, K.; Zakrzewski, V. G.; Voth, G. A.; Salvador, P.; Dannenberg, J. J.; Dapprich, S.; Daniels, A. D.; Farkas, Ö.; Foresman, J. B.; Ortiz, J. V.; Cioslowski, J.; Fox, D. J. Gaussian 09, revision D.01; Gaussian: Wallingford, CT, 2013. Frisch, M. J.; Trucks, G. W.; Schlegel, H. B.; Scuseria, G. E.; Robb, M. A.; Cheeseman, J. R.; Scalmani, G.; Barone, V.; Mennucci, B.; Petersson, G. A.; Nakatsuji, H.; Caricato, M.; Li, X.; Hratchian, H. P.; Izmaylov, A. F.; Bloino, J.; Zheng, G.; Sonnenberg, J. L.; Hada, M.; Ehara, M.; Toyota, K.; Fukuda, R.; Hasegawa, J.; Ishida, M.; Nakajima, T.; Honda, Y.; Kitao, O.; Nakai, H.; Vreven, T.; Montgomery, J. A., Jr.; Peralta, J. E.; Ogliaro, F.; Bearpark, M.; Heyd, J. J.; Brothers, E.; Kudin, K. N.; Staroverov, V. N.; Kobayashi, R.; Normand, J.; Raghavachari, K.; Rendell, A.; Burant, J. C.; Iyengar, S. S.; Tomasi, J.; Cossi, M.; Rega, N.; Millam, N. J.; Klene, M.; Knox, J. E.; Cross, J. B.; Bakken, V.; Adamo, C.; Jaramillo, J.; Gomperts, R.; Stratmann, R. E.; Yazyev, O.; Austin, A. J.; Cammi, R.; Pomelli, C.; Ochterski, J. W.; Martin, R. L.; Morokuma, K.; Zakrzewski, V. G.; Voth, G. A.; Salvador, P.; Dannenberg, J. J.; Dapprich, S.; Daniels, A. D.; Farkas, Ö.; Foresman, J. B.; Ortiz, J. V.; Cioslowski, J.; Fox, D. J. Gaussian 09, revision D.01; Gaussian: Wallingford, CT, 2013.

(8) Becke, A. D. J. Density-Functional Thermochemistry. III. The Role of Exact Exchange. *J. Chem. Phys.* 1993, *98* (7), 5648–5652.

(9) Vosko, S. H.; Wilk, L.; Nusair, M. Accurate Spin-Dependent Electron Liquid Correlation Energies for Local Spin Density Calculations: A Critical Analysis. *Can. J. Phys.* 1980, *58* (8), 1200–1211.

(10) Lee, C.; Yang, W.; Parr, R. G. Development of the Colle-Salvetti Correlation-Energy Formula into a Functional of the Electron Density. *Phys. Rev. B* 1988, *37* (2), 785–789.